PAPER

Persulfate salt as an oxidizer for biocidal energetic nano-thermites†

Wenbo Zhou,[a] Jeffery B. DeLisio,[b] Xiangyu Li,[c] Lu Liu[b] and Michael R. Zachariah*[ab]

Nanoscale potassium persulfate ($K_2S_2O_8$) was evaluated as an alternative to other peroxy salts, such as periodates (KIO_4), in aluminum-fueled energetic nano-composite formulations. High speed imaging coupled with temperature jump (*T*-jump) ignition found the nano-Al/$K_2S_2O_8$ reaction to have an ignition temperature of 600 °C which is comparable to nano-Al/KIO_4 and lower than nano-Al/K_2SO_4. The results from constant-volume pressure cell experiments further show that nano-Al/$K_2S_2O_8$ releases more gas and has a longer burn time than nano-Al/KIO_4. Thermal analyses at low heating rates (10 °C min^{-1}) by coupled differential scanning calorimetry (DSC), thermal gravimetric analysis (TG) and mass spectrometry (MS) show that there are three main steps of thermal decomposition for nano-$K_2S_2O_8$, with initial exothermic decomposition to release O_2 at 270 °C, and following endothermic decomposition to release both O_2 and SO_2 at higher temperatures. The heat of formation of $K_2S_2O_8$ was measured to be -1844.5 kJ mol^{-1} based on the DSC results. Experiments performed at ultrafast heating rates ($\sim10^5$ °C s^{-1}) using temperature-jump time-of-flight (*T*-jump/TOF) MS show that the low O_2 generation temperature of nano-$K_2S_2O_8$ contributes to its high reactivity in nano-thermite compositions. An ignition mechanism involving gaseous oxygen was proposed for nano-thermite compositions containing reactive oxysalts such as nano-$K_2S_2O_8$. In contrast, a condense phase ignition mechanism was proposed for nano-thermites involving less reactive oxysalts such as nano-K_2SO_4. Given that the nano-Al/$K_2S_2O_8$ system is highly exothermic in addition to generating a considerable amount of SO_2, it may be a candidate for use in energetic biocidal applications.

Introduction

Energetic nano-composites, commonly referred to as nano-thermites, are studied for application in propellants, explosives and pyrotechnics due to their rapid exothermic reactions with high energy density.[1–4] For nano-aluminum (Al) fuel based energetic composites, typical oxidizers include nano-sized metal oxides (CuO,[5–7] Fe_2O_3,[8–10] Bi_2O_3,[11,12] *etc.*), oxysalts (NH_4NO_3,[13,14] $NaNO_3$,[15] $NaClO_3$,[16] *etc.*), and the more oxidative peroxy salts (NH_4ClO_4,[17,18] $KClO_4$,[19,20] $NaIO_4$,[21,22] *etc.*). In comparison to metal oxides and oxysalts, peroxy salts possess a higher atomic oxygen content (Table S1†), therefore they typically outperform the aforementioned oxidizers in gas generation and burn rates.[20] Nonmetal–oxygen bonds (Cl–O, I–O, *etc.*) in peroxy salts typically have lower dissociation energies, than metal–oxygen bonds (Cu–O, Fe–O, Bi–O, *etc.*) in metal oxides (Table S1†),[23,24] suggesting a higher oxygen mobility in peroxy salts that can lead to decomposition and oxygen release at lower temperatures. However, the widely used peroxy salt, $KClO_4$, is hygroscopic and has environmental issues, due to the presence of chlorine. These issues have limited its application in many traditional pyrotechnic formulations.[20] A recent study demonstrated that KIO_4, alternatively, has lower toxicity[26] and hygroscopicity[25] making it ideal for applications in illumination and gas generation.[25]

The formal oxidation state of oxygen in each of the aforementioned oxidizers is -2. Exceptional metal peroxides and metal superoxides exist that have higher oxidation states of oxygen (*e.g.* -1 for Na_2O_2 and -0.5 for NaO_2) resulting in stronger oxidation capability. Compared with common metal oxides and peroxy salts whose oxidation capability is based on satiated bonding of oxygen with another element (metal or nonmetal), peroxy compounds with oxidation states greater than -2 feature an oxygen–oxygen bond that has much lower bond dissociation energy[27] resulting in higher oxidative strength (Fig. S1†). More importantly, the intermediate radicals (*e.g.* hydroxyl radical (OH˙)) generated from decomposition of

aDepartment of Chemical and Biomolecular Engineering, University of Maryland, College Park, Maryland, 20742, U.S.A.

bDepartment of Chemistry and Biochemistry, University of Maryland, College Park, Maryland, 20742, U.S.A. E-mail: mrz@umd.edu

cNanjing University of Science and Technology, Nanjing, Jiangsu, 210094, China

† Electronic supplementary information (ESI) available: List of bond energies of M–O in oxidizers and oxygen contents in thermites, molecular structures of oxysalts, spray-drying process of preparing nano-oxysalts, SEM and XRD results of nano-oxysalts, high speed imaging of the wire burning tests, TG/DSC/MS tests of nano-oxysalts, TOF-MS test of nano-Al/K_2SO_4, side reaction of O_2 and SO_2 in the micro-capillary connecting the DSC/TG chamber and MS. See DOI: 10.1039/c5ta00756a

these peroxy compounds in solution are able to initiate a chain of degradation reactions involving other subsequent radicals and oxidants, imposing even higher oxidation ability than the original oxidizers that mainly follow an electron capture based oxidation mechanism.[28–31] As of now, researchers have yet to investigate oxygen–oxygen bond containing oxidizers in the nano-thermite formulations most likely due to the oxidizers being unstable solids at room temperature.[32]

Energetic nano-thermites have been recently investigated for potential widespread neutralization of harmful microorganisms due to recent threats of bio-terrorism[33] and public health issues.[34] Bacterial spores, protected by their multiple self-defending mechanisms, are one of the most resilient and vastly distributed microorganisms.[35,36] Traditionally, two of the most studied and effective inactivation strategies include extreme heat and exposure to biocidal chemicals (*e.g.* iodine and silver).[36] In order to enhance the inactivation efficiency, especially on an emergency basis, dual-function approaches that incorporate biocidals into thermite formulations are attractive as they ideally can generate a lot of heat, and release biocidal agents upon ignition. Zhang *et al.*[37–39] studied a mechanically mixed energetic formulation assembled *via* cryomilling of iodine and aluminum powders, and found the mixture to be thermally stable when the iodine content is below 30% by mass. An alternative manner to incorporate biocidal elements into thermite formulations is through chemical bonding. Both silver oxide (Ag_2O)[40,41] and iodine oxide (I_2O_5)[42–47] have been previously investigated in thermite compositions. Both systems are competitively high in energy density when compared to other high performance metal oxides. In addition, they have exceptional, >60% wt., generation of biocidal products (Ag and I_2) in the aluminum-fueled thermites. Another class of strong oxidizers containing biocidal elements are halogenated oxysalts/peroxysalts such as chlorates/perchlorates and iodates/periodates as mentioned before.[17–22,25] Recently, silver iodate was considered as an oxidizer in a biocidal thermite system.[48] Despite the higher activities of these halogenated (per)oxysalts, neither of the systems produce elemental silver or halogen as a potential biocide.[17–22,25,48]

Considering the challenge of identifying new potential oxysalts capable of generating biocidal products as well as possessing high energy density, an alternative strategy of substituting the halogens in oxysalts with other biocidal elements is employed. Sulfur is widely used as a pesticide[49] and some sulfur-containing species such as sulfur dioxide (SO_2)[50] and sulfuryl fluoride (SO_2F_2)[51] have effective bactericidal and fungicidal properties. A recent report shows that sulfur-containing nanoparticles were able to kill 5 log bacterial spores after 30 min of contact without heating, demonstrating sulfur's strong sporicidal capability.[52] The sporicidal capability of sulfur has not been compared to traditional biocides such as Ag and I_2 despite the large natural abundance of sulfur.[53] Therefore, incorporating sulfur into nano-thermite formulations, especially into peroxy compounds with oxygen–oxygen bonds, demonstrates potential for an effective biocidal energetic material.

Persulfate, which has a symmetrical molecular structure bridging two sulfate groups with an oxygen–oxygen bond (Fig. S1†), shows higher stability at room temperature

analogous to periodate.[25,29] At elevated temperatures, persulfate anions in solution show stronger oxidation capability than permanganate anions[29] and periodate anions,[54] and can trigger the oxidation of a variety of compounds.[28–30] This oxidative priority of persulfate facilitates its wide-range applications in antiseptics and remediation of contamination in nature.[29–31,55–57] Although persulfate displays strong oxidative capabilities in water, it has never been utilized in more violent solid state reactions (*e.g.* thermite reactions).

In this work, potassium persulfate ($K_2S_2O_8$) was chosen as a potential biocidal oxysalt due to its high oxidation state as well as rich content of sulfur. Potassium sulfate (K_2SO_4) and potassium periodate (KIO_4) were employed as controls. These nano-sized oxysalts were prepared using a spray-drying approach. Simultaneous differential scanning calorimetry (DSC), thermal gravimetry (TG) and quadruple mass spectrometry (MS) were performed to investigate the decomposition of $K_2S_2O_8$ nanoparticles at low heating rates. In order to analyze the reaction mechanisms at high heating rates, which more accurately simulate a combustion event, temperature-jump time-of-flight (*T*-jump/TOF) MS was employed. A constant-volume combustion cell was used to evaluate the pressurization rise and optical emission intensity during the combustion of nano-thermites. High speed imaging of the combustion of rapidly heated nano-thermites was also conducted to test the ignition temperatures of these thermite systems.

Experimental section

Preparation of nano-oxysalts and nano-thermites

$K_2S_2O_8$ powders were purchased from Fluka. K_2SO_4 and KIO_4 powders were purchased from Sigma-Aldrich. Al nanopowders were obtained from the Argonide Corporation, and have a size of 50 nm as designated by the supplier.

Nano-sized particles of the oxysalts above were prepared by aerosol spray-drying (Fig. S2†). In detail, 0.47 g $K_2S_2O_8$ as-received powders were dissolved in 100 ml H_2O, which were then sprayed into water droplets of ~1 μm in size[20,25] by ~35 psi pressure air flow. The droplets were first passed through a diffusion dryer to remove most of the water, followed by a tube furnace at 150 °C for complete dehydration. Finally, the nano-particles were collected on a millipore membrane filter (0.4 μm). In the preparation of nano-K_2SO_4 and nano-KIO_4, 0.3 g and 0.4 g of the as-received K_2SO_4 and KIO_4 powders were dissolved in 100 ml H_2O, respectively, followed by the same synthetic route as for nano-$K_2S_2O_8$ with the exception of the furnace temperature being set at 180 °C. The sizes of these three types of nanoparticles were measured by scanning electron microscopy (SEM, Hitachi, SU-70 FEG-SEM). The crystal structures of these nano-oxysalts were confirmed by powder X-ray diffraction (XRD) from a Bruker D8 Advance using Cu Kα radiation.

Three nano-thermite compositions comprised of nano-Al and collected nano-oxysalts above were prepared by mixing these nanoparticles in hexane stoichiometrically and sonicating for 30 min.[20,25] The solvent was then evaporated at room temperature, and the solid nano-thermite powders were collected. It should be

noted that since nano-Al contains a 30% wt alumina (Al_2O_3) shell, the actual weight of nano-Al added was 1.4 times higher.

Constant-volume combustion of nano-thermite reactions

A constant-volume combustion cell was used to study the pressurization and optical emission during the nano-thermite reactions. 25 mg of nano-thermite sample was loaded inside the ~ 13 cm^3 combustion cell in air. Ignition was initiated *via* a resistively heated nichrome coil resting on top of the sample, and the temporal pressure and optical emission from the nano-thermite reaction were measured by using a piezoelectric pressure sensor and a photodetector, respectively. Each experiment was repeated at least twice. More details of the experiment can be found in ref. 25.

Nano-oxysalts and nano-thermites at ultrafast heating rates

T-jump/TOF MS was employed to analyse the evolution of gaseous species during the decomposition of nano-$K_2S_2O_8$ at ultrafast heating rates of $\sim 10^5$ °C s^{-1}. Nano-$K_2S_2O_8$ powders were dispersed in hexane and ultrasonicated for 30 min and then deposited onto a 76 μm Pt wire. The coated mass on the wire was controlled around 90 μg.[25] The Pt wire was then inserted into the MS chamber where it is rapidly joule-heated to ~ 1200 °C by a 3 ms pulse. The current and voltage signals were recorded and the temporal temperature on the wire was measured according to the Callendar–Van Dusen equation. MS spectra were measured every 0.1 ms. For the detailed experimental set-up, please see ref. 58.

In order to determine the ignition temperatures of thermite mixtures in different environments, a Vision Research Phantom v12.0 high speed camera (14.9 μs per frame) was used to monitor the combustion on the wire during heating. Ignition temperatures of nano-thermite reactions in vacuum were measured from the correlation of optical emission from high speed imaging and temporal temperature of the wire, and were further analyzed in combination with the temporal mass spectra. Ignition temperatures in air and in Ar at atmospheric pressure were also measured in a separate home-built chamber. Each experiment was repeated 3 times.

Thermal decomposition of nano-oxysalts at lower heating rates

DSC, TG, and MS tests were conducted simultaneously in a SDT Q600 coupled to a DiscoveryTM quadruple mass spectrometer from TA Instruments, U.S.A. Around 2 mg of nano-$K_2S_2O_8$ was loaded into the sample crucible inside the apparatus and heated at 10 °C min^{-1} in 100 l min^{-1} Ar flow up to 1400 °C. A heated micro-capillary (~ 300 °C) connects the SDT Q600 chamber to the MS, enabling transport of the thermally decomposed species to the MS detector. The linear relationship between the concentration of gas species i (C_i) and its ion intensity (I_i) detected from MS is:[59]

$$I_i = K\sigma_i C_i \qquad (1)$$

where K is the instrumental constant and σ_i is the electron-impact ionization cross-section of species i (O_2, SO_2 or Ar). Ar was used as an internal standard to determine the effective instrumental response factor. At an incident energy of 70 eV in our MS system, the ionization cross-sections for O_2, SO_2 and Ar are 2.4 Å^2, 5.0 Å^2, and 10.0 Å^2, respectively.[60] Given that I_i can be measured and C_{Ar} was known by the Ar flow rate, the concentrations of O_2 (C_{O_2}) and SO_2 (C_{SO_2}) can be theoretically measured through eqn (2):

$$C_i = \frac{I_i \sigma_{Ar} C_{Ar}}{I_{Ar} \sigma_i} \qquad (2)$$

Finally, the net quantities of O_2 and SO_2 can be measured by integration of C_i over time.

Results and discussion

Analysis of prepared nano-oxysalts and nano-thermites

All of the as-received oxysalt powders are micro-sized in a wide size range. The average particle sizes are 40.7 μm, 33.7 μm and 21.9 μm for $K_2S_2O_8$, K_2SO_4 and KIO_4 powders, respectively (Fig. 1A, S3A and S3B†). Nano-sized oxysalts were prepared by spray-drying of aqueous oxysalt solutions (Fig. S2†). The average sizes of nano-oxysalts are 0.46 ± 0.19 μm, 0.42 ± 0.24 μm, and 0.46 ± 0.27 μm for nano-$K_2S_2O_8$, nano-K_2SO_4, and nano-KIO_4, respectively (Fig. 1B, S3C and S3D†). The average particle sizes above were determined by SEM images based on >100 particle counts.

Nano-thermites were prepared by sonicating the mixture of nano-oxysalts and nano-Al in hexane. Although the size of the nano-$K_2S_2O_8$ is 10 times larger than that of nano-Al, there is still intimate contact as seen in the SEM image of the nano-thermite mixture (Fig. 1C).

Ignition of nano-thermites

The ignition of nano-thermites at high heating rates was characterized in the *T*-jump heating experiments monitored by using a high-speed camera. The time-resolved light intensities were measured using the high speed videos (Fig. S4†), and the ignition times were identified as the points where light intensities begin to increase (Fig. 2). These ignition times correlate with the time resolved wire temperatures to determine the ignition temperatures for the nano-thermite compositions. Fig. 2A shows that the nano-Al/$K_2S_2O_8$ has an ignition temperature of 595 ± 22 °C in Ar, which is similar to that of nano-Al/KIO_4 (600 ± 27 °C), but much lower than that of nano-Al/K_2SO_4 (805 ± 15 °C). The large temperature difference demonstrates that nano-$K_2S_2O_8$ and nano-KIO_4 are more reactive in the aluminum-fueled thermites than nano-K_2SO_4. This result also indicates that the oxygen in nano-$K_2S_2O_8$ and nano-KIO_4 were able to react with Al at temperatures where Al is still solid, while nano-K_2SO_4 reacts with the Al melt (>660 °C). In open air, ignition temperatures of both nano-Al/$K_2S_2O_8$ and nano-Al/KIO_4 were around 600 °C (Fig. 2B), which are equivalent to their ignition temperatures in Ar. This alludes to the fact that although the O_2 in air may play a role in the overall reaction, it
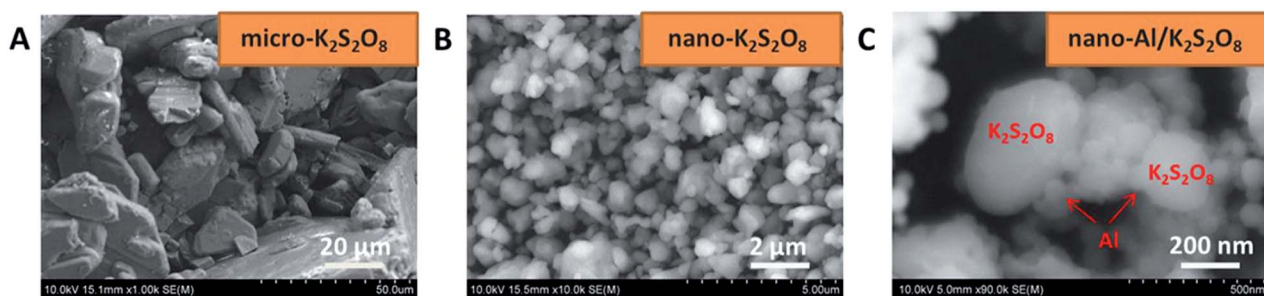
Fig. 1 (A) SEM of the as-received micro-sized $K_2S_2O_8$; (B) SEM of nano-sized $K_2S_2O_8$ prepared by spray-drying of $K_2S_2O_8$ solutions; (C) SEM of nano-thermite formulation of nano-Al and nano-$K_2S_2O_8$.
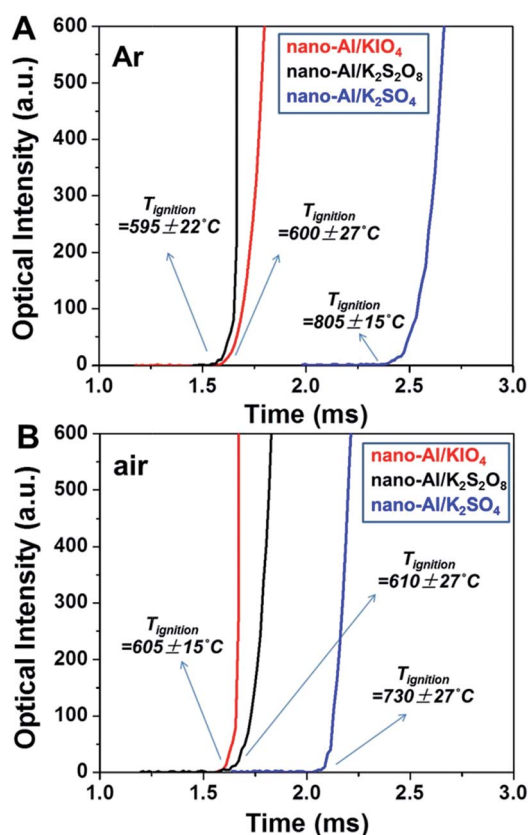

Fig. 2 Time-resolved optical intensity profiles of nano-Al/$K_2S_2O_8$, nano-Al/KIO_4, and nano-Al/K_2SO_4 thermite reactions in Ar (A) and in air (B). Optical intensities were measured from high-speed camera videos. The ignition temperatures of thermite reactions are labelled. The heating rate is $\sim4 \times 10^5$ °C s^{-1}.

does not have an impact on the ignition process for these systems. This also indicates that nano-$K_2S_2O_8$ and nano-KIO_4 were able to provide a higher transient concentration of reactive oxygen species around the Al nanoparticles, ensuring ignition at temperatures approaching the melting point of Al where Al becomes highly mobile and diffuses outwards through the oxide shell. Conversely, the ignition temperature of nano-Al/K_2SO_4 (730 ± 27 °C) in air is lower than that in Ar (805 ± 15 °C), suggesting that the gaseous oxygen in air augmented the ignition by reacting with the Al melt. The reactivity of the nano-Al/

$K_2S_2O_8$ and nano-Al/KIO_4 thermites in vacuum (data not shown), showed overall weak optical emission and higher ignition temperatures ($\sim$740 °C). At the low pressure used in these experiments ($\sim10^{-7}$ Torr), gaseous oxygen if released from the oxidizer, will have little time to interact with the fuel and we should expect a delayed ignition. This suggests that for the persulfate in the initiation process is not a condensed phase reaction between solid Al and bound oxygen in solid $K_2S_2O_8$, but initiated by the reaction between solid Al and gaseous O_2 released from $K_2S_2O_8$.

Pressurization and optical emission of nano-thermite reactions

Pressurization rate and burn time were measured using sample masses 2 orders of magnitude larger than what is required for the T-jump ignition experiments above (25 mg vs. 0.09 mg). The results from the constant-volume combustion cell tests (Fig. 3A) show that the pressurization rate and maximum pressure in the nano-Al/$K_2S_2O_8$ reaction are 151 ± 26 kPa μs^{-1} and 1206 ± 208 kPa, respectively, which are considerably higher than the reported pressurization rate and maximum pressure in the standard nano-thermite reaction of Al/CuO (V_p = 60 kPa μs^{-1}, P_{max} = 700 kPa).[20] Previously, it was reported that the nano-Al/KIO_4 reaction possessed the highest measured pressurization rate per mole of Al.[25] The nano-Al/$K_2S_2O_8$ reaction convincingly demonstrates a higher pressurization rate and peak pressure exceeding those of the nano-Al/KIO_4 reaction (V_p = 91 ± 19 kPa μs^{-1}, P_{max} = 909 ± 185 kPa) (Fig. 3A). A simple explanation for the higher pressurization in the nano-Al/$K_2S_2O_8$ reaction than the other nano-Al/oxysalt reactions is its high content of oxygen per mass of thermite (31%) (Table S1†). Nano-Al/K_2SO_4 thermite has a little smaller oxygen content (26%) when compared to the nano-Al/$K_2S_2O_8$ thermite (Table S1†), though the difference observed in peak pressures during the reaction is much larger (Fig. 3A). This result implies that the pressurization observed in a thermite reaction is also dependent on the available oxygen that can be released from the oxysalt.

The burn time of the thermite reactions, which is defined as the full width at half maximum of the optical emission peak, was detected in the combustion cell tests (Fig. 3B). Fig. 3B shows that the nano-Al/$K_2S_2O_8$ reaction has a 2-fold higher optical emission, as well as burn time, than the nano-Al/KIO_4
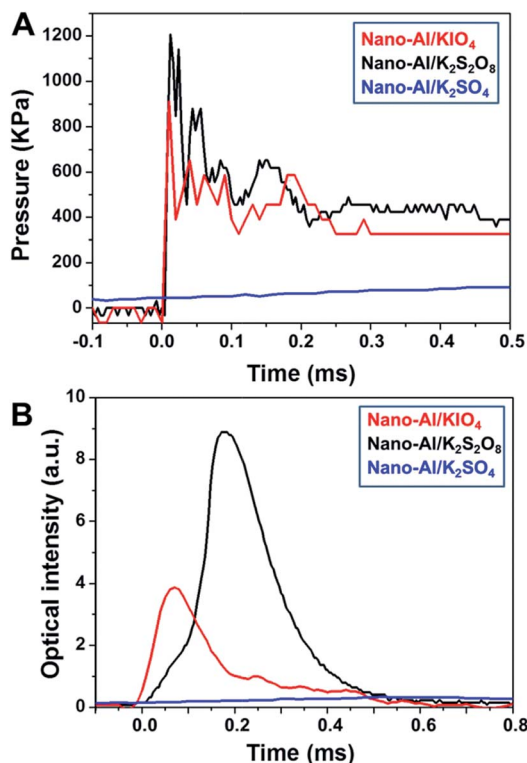
Fig. 3 Temporal pressure (A) and optical intensity (B) in the combustion cell tests of nano-thermites including nano-Al/$K_2S_2O_8$, nano-Al/KIO_4, and nano-Al/K_2SO_4, respectively. The temporal pressure in (A) represents the pressure increase from 1 atm.

reaction despite the nano-Al/KIO_4 reaction showing a higher optical emission rate. This result indicates that although the nano-Al/KIO_4 thermite burns faster, the nano-Al/$K_2S_2O_8$ thermite provides more optically intensive (higher temperature), longer sustained combustion. While nano-Al/$K_2S_2O_8$ behaves superior to nano-Al/KIO_4 in this metric, both reactions show much stronger optical emission than nano-Al/K_2SO_4 (Fig. 3B). Furthermore the nano-Al/$K_2S_2O_8$ thermite is still one of the fastest burning species we have measured and second only to nano-Al/KIO_4. The pressurization and optical emission results for all the three thermite systems are presented in Table 1. In general, from both pressurization and combustion intensity, as determined by light emission, nano-$K_2S_2O_8$ is a far more effective oxidizer in the aluminum-fueled thermite.

Table 1 Pressurization rates (V_p), maximum pressures (P_{max}), burn times (T_{burn}), and maximum optical intensities (I_{max}) of the thermite reactions of nano-Al/$K_2S_2O_8$, nano-Al/KIO_4, and nano-Al/K_2SO_4 in the combustion cell tests. P_{max} represents the maximum pressure increase from 1 atm

Nano-thermites	V_p (kPa μs^{-1})	P_{max} (kPa)	T_{burn} (μs)	I_{max} (V)
Nano-Al/$K_2S_2O_8$	151 ± 26	1206 ± 208	205 ± 38	9.0 ± 1.9
Nano-Al/KIO_4	91 ± 19	909 ± 185	130 ± 35	4.0 ± 0.5
Nano-Al/K_2SO_4	0.06 ± 0.02	104 ± 14	2800 ± 400	0.3 ± 0.1

It should be noted that the timescales of pressurization and optical emission are different. In both nano-Al/$K_2S_2O_8$ and nano-Al/KIO_4 reactions, the time required to reach peak pressure (8–10 μs) was about one tenth of their burn times (T_{burn} = 205–130 μs), suggesting that product gas is generated from the oxysalts prior to the start of ignition and combustion. Thus, the gaseous reactive oxygen species that initiate ignition of the thermite may be from the product gas. Distinctively, for the nano-Al/K_2SO_4 reaction, the burn time is comparable to the time to reach maximum pressure (>1 ms) (Table 1), suggesting that gas is generated during the ignition process.

Thermal decomposition pathways of nano-oxysalts at low heating rates

The characterization of ignition and combustion of the three nano-thermites both in small and large reaction scales demonstrates that the thermite reactivity and energy density are strongly dependent on the oxysalt used. Thermal and mass analyses of the decomposition of oxysalts can provide the energetics of the reaction, as well as decomposition products and global pathways, which can be connected to the ignition and pressurization mechanism. At a low heating rate of 10 °C min^{-1}, the TG, DSC and MS profiles for nano-$K_2S_2O_8$ show several sequential mass and enthalpy changes (step a–f) (Fig. 4 and S5†). The nano-$K_2S_2O_8$ was first dehydrated below 270 °C with a mass loss of 0.6% (Fig. 4A). Importantly this degree of hygroscopicity when compared with other oxysalts such as KIO_4 (17.66%, see Fig. S5A†) is negligible. Starting from 270 °C, the nano-$K_2S_2O_8$ predominantly underwent three decomposition steps. The first step is the decomposition of $K_2S_2O_8$ to $K_2S_2O_7$ and O_2, which shows two mass reduction sub-steps at 270 °C and 310 °C (Fig. 4A), indicating bimodal oxygen release peaks (Fig. 4C). The measured quantity of released O_2 from MS (0.125 mg) (Fig. 4C) is consistent with the mass reduction of the nano-$K_2S_2O_8$ loaded (2 mg × 5.8% = 0.116 mg) (Fig. 4A), confirming that O_2 is the only product gas at this stage. DSC results show that this step is highly exothermic (-288 J g^{-1} $-$ 17.1 J g^{-1} = -305.1 J g^{-1}) (Fig. 4B and Table 2, see detailed enthalpy analysis in the ESI†). Given that most metal oxide and oxysalt decompositions are endothermic,[25] the exothermicity of nano-$K_2S_2O_8$'s decomposition would presumably ensure better reactivity in a thermite composition. A similar phenomenon has been previously published for nano-KIO_4,[25] although the exothermicity is less than half of what is observed for nano-$K_2S_2O_8$ (-121 J g^{-1}, Fig. S5B†).

The second step is the decomposition of $K_2S_2O_7$ to K_2SO_4, SO_2, and O_2 at 440 °C as confirmed by TG (Fig. 4A) and MS (Fig. 4C and D) results. It should be noted that the molar quantities of O_2 and SO_2 detected in MS (Fig. 4C and D) are much smaller than those quantities measured from the mass reduction in TG (Fig. 4A). The likely reason for the discrepancy is that SO_2, as it passes through the much cooler micro-capillary (~300 °C), undergoes a reaction yielding sulfuric acid. The detailed explanation of this side reaction, as well as the rationalization of high conversion of O_2 and SO_2, can be found in the ESI.†
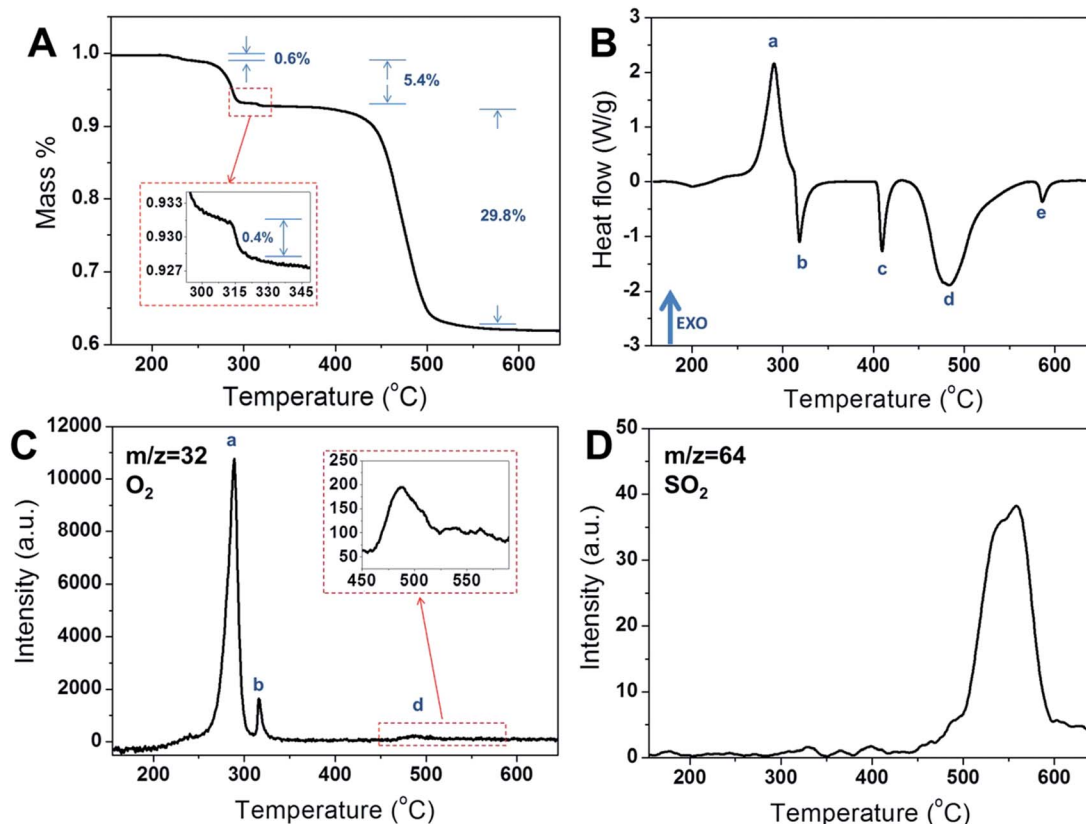
11842 | *J. Mater. Chem. A*, 2015, **3**, 11838–11846

This journal is © The Royal Society of Chemistry 2015

Fig. 4 TG (A), DSC (B) and MS for O_2 (C, $m/z = 32$) and SO_2 (D, $m/z = 64$) profiles of $K_2S_2O_8$ in the temperature range from room temperature to 645 °C. The heating rate is 10 °C min^{-1}.

Table 2 Thermal decomposition steps of nano-$K_2S_2O_8$ from TG, DSC and MS tests at a heating rate of 10 °C min^{-1}

Steps	T_{onset} (°C)	Physiochemical changes	ΔH (J g^{-1})
a	270	$K_2S_2O_8(s) = K_2S_2O_7(s) + 0.5\ O_2$ (most)	−288
b	310	$K_2S_2O_8(s) = K_2S_2O_7(s) + 0.5\ O_2$	−17.1
		$K_2S_2O_7(s) = K_2S_2O_7(s)$ (phase change)	81.3
c	405	$K_2S_2O_7(s) = K_2S_2O_7(l)$ (melting)	61.8
d	450	$K_2S_2O_7(l) = K_2SO_4(s) + 0.5\ O_2 + SO_2$	570
e	580	$K_2SO_4(s) = K_2SO_4(s)$ (phase change)	13.3
f[a]	1110	$K_2SO_4(s) = 2K + O_2 + SO_2$	5463

[a] This reaction equation was implied from the MS results. The exact products are unknown.

The final decomposition step began at ~1200 °C (Fig. S6A†) and its temperature range exceeded the upper limit of our TG temperature capabilities, rendering it difficult to deduce the decomposition route. However, the emergence of both SO_2 and O_2 in MS (Fig. S6C and S6D†) suggests that the reaction is from K_2SO_4 to SO_2, O_2, and K, which is also confirmed by other reports.[61]

The following multi-step decomposition of nano-$K_2S_2O_8$ is proposed based on the TG/DSC/MS results as summarized in Table 2. XRD results further confirm the main products ($K_2S_2O_7$ and K_2SO_4) during heating of nano-$K_2S_2O_8$ (Fig. 5). Compared to other oxysalts such as KIO_4 and K_2SO_4, $K_2S_2O_8$ possesses the lowest oxygen release temperature at 270 °C (vs. 330 °C for KIO_4 and 1200 °C for K_2SO_4), as well as the highest exothermic heat of −305.1 kJ g^{-1} (vs. −120.5 kJ g^{-1} for KIO_4), thus confirming

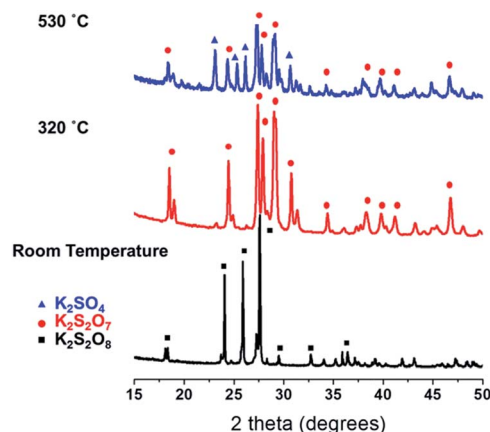Fig. 5 XRD profiles of prepared nano-$K_2S_2O_8$ (A) and nano-$K_2S_2O_8$ after heating to 320 °C (B) and 530 °C (C). The marks above the major peaks represent the positions of reflection corresponding to the triclinic $K_2S_2O_8$ phase (JCPDS no.: 32-0846), monoclinic $K_2S_2O_7$ phase (JCPDS no.: 22-1239) and K_2SO_4 phase (JCPDS no.: 05-0613). Some of the minor peaks in the room temperature pattern probably belong to impurities like SiO_2 from the diffusion dryer.

better ignition and combustion performance in the thermite reaction as shown in Fig. 2 and 3. Furthermore, 4 moles of gas (including O_2 and SO_2) were generated per mole of $K_2S_2O_8$ (Table 2), which is a factor of 2 more than per mole of KIO_4, indicating $K_2S_2O_8$ as a better gas generator.

Given that the heat of reaction in each step was quantified (Table 2), as well as the standard heat of formation of solid K_2SO_4 and gaseous SO_2 (-1437.7 kJ mol^{-1} and -296.8 kJ mol^{-1} respectively),[60] we can deduce the heat of formation of $K_2S_2O_8$ from (combing equations in step a–d):

$$K_2S_2O_8 \rightarrow K_2SO_4 + SO_2 + O_2 \tag{3}$$

We obtain: ΔH_f $K_2S_2O_8 = -1844.5$ kJ mol^{-1}.

The global equation (from $K_2S_2O_8$ to SO_2, O_2, and K) was not used for this calculation because of the uncertainty in final products as previously mentioned.

Thermal decomposition of nano-oxysalts at ultrafast heating rates

To further evaluate nano-$K_2S_2O_8$ as an oxidizer in an energetic composition, high heating rate analytics that will more accurately represent timescales of a combustion event were employed. *T*-jump/TOF MS at a heating rate of $\sim 4 \times 10^5$ °C s^{-1} was used to obtain time resolved spectra at 0.1 ms intervals that could be further analysed to determine the signal intensity over time of O_2, SO_2 and K (Fig. 6). Similar to the mass spectra at low heating rates (Fig. 4C and D), the decomposition of nano-$K_2S_2O_8$ also undergoes three major steps. The initial step has an onset temperature of 335 °C (Fig. 6A), where oxygen is generated from the decomposition of $K_2S_2O_8$ to $K_2S_2O_7$ (Table 2). This onset temperature is higher than that in the TG/DSC result (Fig. 4) due to the employment of a much higher heating rate ($\sim 10^5$ °C s^{-1} *vs.* 10 °C min^{-1}). At a higher temperature of 435 °C, SO_2, in addition to a second release of O_2, was detected (Fig. 6A and B) representing the second step of decomposition from $K_2S_2O_7$ to K_2SO_4 (Table 2). The final decomposition step occurs at 710 °C where O, SO_2 and K were detected in the MS (Fig. 6A–C). Based on the similarity between the thermal decomposition of nano-$K_2S_2O_8$ at ultrafast heating rates and low heating rates (Table 2), we propose that the thermal decomposition mechanism of nano-$K_2S_2O_8$ appears to be independent of heating rate. However, the oxygen intensity ratio of step 1 and step 2 in the ultrafast heating result (Fig. 6) is much lower than what is observed in the low heating result (Table 2), indicating that some $K_2S_2O_8$ did not decompose at the lower temperature in step 1. This could be due to the inhomogeneity of nano-$K_2S_2O_8$ (surface *vs.* bulk) in its first decomposition process to $K_2S_2O_7$, which also leads to the bimodal oxygen peaks as we see in the TG-MS results (Fig. 4A and C). The likely reason for only one initial O_2 release peak at higher heating rates (Fig. 6A) is that the decomposition time from $K_2S_2O_8$ to $K_2S_2O_7$ ($\sim 10^2$ s, estimated from Fig. 4C) is much longer than the heating time in step 1 ($\sim 10^{-3}$ s, Fig. 6A), which results in incomplete decomposition of $K_2S_2O_8$ in step 1.

Decomposition of nano-K_2SO_4 (Fig. S7A†) shows that no oxygen was detected until 840 °C, with the appearance of SO_2 and K at ~ 1000 °C. In contrast we found that K_2SO_4 generated
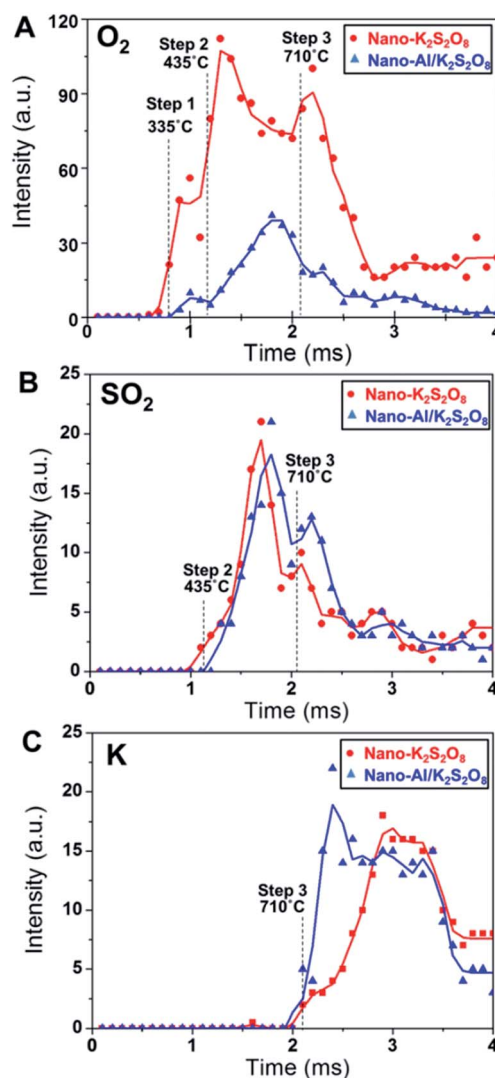

Fig. 6 (A–C) are TOF-MS temporal profiles of oxygen, sulfur dioxide and potassium release, respectively, during a 3 ms pulse heating. Measured mass intensity data at each time point are denoted as circles for decomposition of nano-$K_2S_2O_8$, and triangles for the thermite reaction of nano-Al/$K_2S_2O_8$, respectively. The starting temperatures for select MS peaks are shown.

from the decomposition of $K_2S_2O_8$ has a lower onset decomposition temperature at 710 °C (Fig. 6). This temperature difference suggests that the gas generation in the previous steps of $K_2S_2O_8$ decomposition facilitates the further decomposition of the K_2SO_4 product.

Nano-thermite reaction at ultrafast heating rates

For evaluating the thermite performance of nano-$K_2S_2O_8$ under high heating rate conditions, *T*-jump/TOF MS was employed to analyse the reaction between nano-$K_2S_2O_8$ and nano-Al in a stoichiometric physical mixture. Fig. 6 shows that both nano-thermite and thermal decomposition of nano-$K_2S_2O_8$ have an initial oxygen release peak at 335 °C. Starting from 470 °C, significant oxygen release was detected, though the intensity is lower than that in the decomposition of nano-$K_2S_2O_8$ (Fig. 6A).

SO_2 was also released at this stage, with an onset temperature (435 °C) similar to what is observed in the pure oxidizer case (Fig. 6B). The similarity in SO_2 profiles implies that the produced SO_2 did not further react with Al, which was confirmed by the product analysis that showed no Al_2S_3. At higher temperature >710 °C at which a third decomposition step commenced for nano-$K_2S_2O_8$, K was detected with a similar intensity to that in the pure oxidizer case (Fig. 6C), implying that K did not participate in the reaction with Al. In this step, very little oxygen was detected in the thermite reaction (Fig. 6A) indicating that negligible intermediate product K_2SO_4 was generated.

The reactive oxygen species that initiate the reaction addressed in the ignition and pressure cell tests (Fig. 2 and 3) are suggested to be gaseous species released from $K_2S_2O_8$ decomposition as opposed to oxygen species in the solid oxy-salts, or background O_2 if combusted in air. Direct evidence for this proposition is that the ignition occurs at a lower temperature when rapidly heated in argon at 1 atm as opposed to being heated at low pressures. There is a higher local concentration of reactive oxygen species near the aluminum fuel when heated at higher pressures. Thus, the thermite ignition is proposed to be initiated by the generated gaseous oxygen species reacting with solid Al at the surface of Al particles. However, nano-Al/$K_2S_2O_8$ and nano-Al/KIO_4 thermites have different oxygen release temperatures of 335 °C (Fig. 6A) and 470 °C (ref. 25) respectively, but they have similar ignition temperatures in Ar (600 °C, see Fig. 2). This indicates that the mobilization of Al, which increases as the melting point of Al (660 °C) is approached, plays a more important role in controlling ignition than the gaseous reactive oxygen generated from the decomposition of oxysalts.

In contrast, nano-Al/K_2SO_4 has higher oxygen release temperature (840 °C, see Fig. S7B†) than both its ignition temperature in Ar (805 °C, see Fig. 2) and melting point of Al. Gas generation is negligible in this case (Fig. 3B and S7B†), suggesting that the reaction mechanism for this type of inactive oxysalt mainly undergoes a condensed phase route resembling the case for many metal oxides.[62,63]

It is important to note in the end that when compared to the decomposition of nano-KIO_4, nano-$K_2S_2O_8$ generates gaseous SO_2 thus ensuring the production of this biocidal gas during the thermite reaction (Fig. 6B). Bearing in mind that SO_2 is the major sulfur-containing products from the thermite reaction, the amount of biocidal SO_2 produced from the thermite reaction is estimated to be 31% by mass for nano-Al/$K_2S_2O_8$, which is higher than that for nano-Al/K_2SO_4 (26%) and nano-Al/KIO_4 (0%). Due to the high biocidal gas productivity as well as the super-reactive thermite performance, nano-$K_2S_2O_8$ can be used to formulate promising biocidal energetic nano-composites.

Conclusions

In this study, potassium persulfate was evaluated as an oxidizer in energetic aluminum-fueled nano-composite formulations for its possible biocidal deployment through the release of SO_2. The nano-Al/$K_2S_2O_8$ reaction has a low ignition temperature (600 °C)

in Ar or air when compared to other nano-thermite compositions, and demonstrates combustion performance comparable to nano-Al/KIO_4. Constant-volume pressure cell results further show that the nano-Al/$K_2S_2O_8$ produces more gas than the nano-Al/KIO_4 and has a longer burn time indicating a more persistent combustion feature. Three major steps in the thermal decomposition for the nano-$K_2S_2O_8$ were identified including a low temperature exothermic peak corresponding to the release of oxygen at 270 °C, as well as the release of sulfur dioxide at 450 °C.

We determined that the ignition of nano-Al/$K_2S_2O_8$ is controlled by the reaction between gaseous oxygen and mobilized Al. These experimental results demonstrate that the nano-thermite formulation consists of nano-Al/$K_2S_2O_8$ features both high exothermicity and biocidal gas generation, making it an optimal candidate for use in energetic biocidal applications.

Acknowledgements

Notes and references

1 R. A. Yetter, G. A. Risha and S. F. Son, *Proc. Combust. Inst.*, 2009, **32**, 1819–1838.
2 E. L. Dreizin, *Prog. Energy Combust. Sci.*, 2009, **35**, 141–167.
3 N. H. Yen and L. Y. Wang, *Propellants, Explos., Pyrotech.*, 2012, **37**, 143–155.
4 C. Rossi, *Propellants, Explos., Pyrotech.*, 2014, **39**, 323–327.
5 S. Apperson, R. V. Shende, S. Subramanian, D. Tappmeyer, S. Gangopadhyay, Z. Chen, K. Gangopadhyay, P. Redner, S. Nicholich and D. Kapoor, *Appl. Phys. Lett.*, 2007, **91**, 243109.
6 D. K. Kim, J. H. Bae, M. K. Kang and H. J. Kim, *Curr. Appl. Phys.*, 2011, **11**, 1067–1070.
7 J. Wang, A. Hu, J. Persic, J. Z. Wen and Y. N. Zhou, *J. Phys. Chem. Solids*, 2011, **72**, 620–625.
8 J. Mei, R. D. Halldearn and P. Xiao, *Scr. Mater.*, 1999, **41**, 541–548.
9 T. M. Tillotson, A. E. Gash, R. L. Simpson, L. W. Hrubesh, J. H. Satcher Jr. and J. F. Poco, *J. Non-Cryst. Solids*, 2001, **285**, 338–345.
10 L. Menon, S. Patibandla, K. Bhargava Ram, S. I. Shkuratov, D. Aurongzeb, M. Holtz, J. Berg, J. Yun and H. Temkin, *Appl. Phys. Lett.*, 2004, **84**, 4735–4737.
11 J. A. Puszynski, C. J. Bulian and J. J. Swiathiewiz, *J. Propul. Power*, 2007, **23**, 698–706.
12 K. S. Martirosyan, L. Wang, A. Vicent and D. Luss, *Nanotechnology*, 2009, **20**, 405609.
13 R. Thiruvengadathan, A. Bezmelnitsyn, S. Apperson, C. Staley, P. Redner, W. Balas, S. Nicholich, D. Kapoor, K. Gangopadhyay and S. Gangopadhyay, *Combust. Flame*, 2011, **158**, 964–978.
14 W. K. Lewis, B. A. Harruff, J. R. Gord, A. T. Rosenberger, T. M. Sexton, E. A. Guliants and C. E. Bunker, *J. Phys. Chem. C*, 2011, **115**, 70–77.

15 S. Umbrajkar, M. A. Trunov, M. Schoenitz and E. L. Dreizin, *Propellants, Explos., Pyrotech.*, 2007, **32**, 32–41.

16 M. A. Machado, D. A. Rodriguez, Y. Aly, M. Schoenitz, E. L. Dreizin and E. Shafirovich, *Combust. Flame*, 2014, **161**, 2708–2716.

17 R. W. Armstrong, B. Bschung, D. W. Booth and M. Samirant, *Nano Lett.*, 2003, **3**, 253–255.

18 A. N. Pivkina, Y. V. Frolov and D. A. Ivanov, *Combust. Explos. Shock Waves*, 2007, **43**, 51–55.

19 X. Kang, J. Zhang, Q. Zhang, K. Du and Y. Tang, *J. Therm. Anal. Calorim.*, 2012, **109**, 1333–1340.

20 C. Wu, K. Sullivan, S. Chowdhury, G. Jian, L. Zhou and M. R. Zachariah, *Adv. Funct. Mater.*, 2012, **22**, 78–85.

21 C. R. Becker, S. Apperson, C. J. Morris, S. Gangopadhyay, L. J. Currano, W. A. Churaman and C. R. Stoldt, *Nano Lett.*, 2011, **11**, 803–807.

22 J. C. Poret, A. P. Shaw, C. M. Csernica, K. D. Oyler, J. A. Vanatta and G. Chen, *ACS Sustainable Chem. Eng.*, 2013, **1**, 1333–1338.

23 Y. R. Luo, *Comprehensive Handbook of Chemical Bond Energies*, CRC Press, Boca Raton, FL, 2007.

24 B. D. Darwent, Bond Dissociation Energies in Simple Molecules, *Natl. Stand. Ref. Data Ser.*, 1970, **31**, 1–52.

25 G. Jian, J. Feng, R. J. Jacob, G. C. Egan and M. R. Zachariah, *Angew. Chem., Int. Ed.*, 2013, **52**, 1–5.

26 J. A. Conkling and C. J. Mocella, *Chemistry of Pyrotechnics: Basic Principles and Theory*, 2nd edn, CRC Press-Taylor & Francis Group, Boca Raton, 2010, pp. 69–70.

27 R. T. Sanderson, *Chemical Bonds and Bond Energy*, Academic Press, New York, 1971.

28 I. M. Kolthoff and I. K. Miller, *J. Am. Chem. Soc.*, 1951, **73**, 3055–3059.

29 K.-C. Huang, R. A. Couttenye and G. E. Hoag, *Chemosphere*, 2002, **49**, 413–420.

30 R. H. Waldemer, P. G. Tratnyek, R. L. Johnson and J. T. Nurmi, *Environ. Sci. Technol.*, 2007, **41**, 1010–1015.

31 A. Tsitonaki, B. Petri, M. Crimi, H. Mosbæk, R. L. Siegrist and P. L. Bjerg, *Crit. Rev. Environ. Sci. Technol.*, 2010, **40**, 55–91.

32 F. A. Cotton and G. Wilkinson, *Advance Iorganic Chemistry*, 3rd edn, John Wiley & Sons, New York, 1972.

33 E. Nadasi, T. Varjas, I. Prantner, V. Virag and I. Ember, *Gene Ther. Mol. Biol.*, 2007, **11**, 315–320.

34 Y. Gilbert and C. Duchaine, *Can. J. Civ. Eng.*, 2009, **36**, 1873–1886.

35 W. L. Nicholson, N. Munakata, G. Horneck, H. J. Melosh and P. Setlow, *Microbiol. Mol. Biol. Rev.*, 2000, **64**, 548–572.

36 P. Setlow, *J. Appl. Microbiol.*, 2006, **101**, 514–525.

37 S. Zhang, M. Schoenitz and E. L. Dreizin, *J. Phys. Chem. Solids*, 2010, **71**, 1213–1220.

38 S. Zhang, M. Schoenitz and E. L. Dreizin, *J. Phys. Chem. C*, 2010, **114**, 19653–19659.

39 S. Zhang, C. Badiola, M. Schoenitz and E. L. Dreizin, *Combust. Flame*, 2012, **159**, 1980–1986.

40 R. Russell, S. Bless and M. Pantoya, *J. Energ. Mater.*, 2011, **29**, 175–192.

41 K. T. Sullivan, C. Wu, N. W. Piekiel, K. Gaskell and M. R. Zachariah, *Combust. Flame*, 2013, **160**, 438–446.

42 K. S. Martirosyan, L. Wang and D. Luss, *Chem. Phys. Lett.*, 2009, **483**, 107–110.

43 B. R. Clark and M. L. Pantoya, *Phys. Chem. Chem. Phys.*, 2010, **12**, 12653–12657.

44 C. Farley and M. Pantoya, *J. Therm. Anal. Calorim.*, 2010, **102**, 609–613.

45 C. W. Farley, M. L. Pantoya, M. Losada and S. Chaudhuri, *J. Chem. Phys.*, 2013, **139**, 074701.

46 J. Feng, G. Jian, Q. Liu and M. R. Zachariah, *ACS Appl. Mater. Interfaces*, 2013, **5**, 8875–8880.

47 O. Mulamba and M. Pantoya, *J. Nanopart. Res.*, 2014, **16**, 2310.

48 K. T. Sullivan, N. W. Piekiel, S. Chowdhury, C. Wu, M. R. Zachariah and C. E. Johnson, *Combust. Sci. Technol.*, 2011, **183**, 285–302.

49 K. J. Rao and S. Paria, *RSC Adv.*, 2013, **3**, 10471.

50 L. Palou, C. H. Crisosto, D. Garner, L. M. Basinal, J. L. Smilanick and J. P. Zoffoli, *Am. J. Enol. Vitic.*, 2002, **53**, 110–115.

51 V. C. Papadimitriou, R. W. Portmann, D. W. Fahey, J. Muhle, R. F. Weiss and J. B. Burkholder, *J. Phys. Chem. A*, 2008, **112**, 12657–12666.

52 D. B. Hamal, J. A. Haggstrom, G. L. Marchin, M. A. Ikenberry, K. Hohn and K. J. Klabunde, *Langmuir*, 2010, **26**, 2805–2810.

53 S. R. Choudhury, M. Ghosh, A. Mandal, D. Chakravorty, M. Pal, S. Pradhan and A. Goswami, *Appl. Microbiol. Biotechnol.*, 2011, **90**, 733–743.

54 G. L. Cohen and G. Atkinson, *Inorg. Chem.*, 1964, **3**, 1741–1743.

55 C. Liang, C. J. Bruell, M. C. Marley and K. L. Sperry, *Chemosphere*, 2004, **55**, 1213–1223.

56 S.-Y. Oh, H.-W. Kim, J.-M. Park, H.-S. Park and C. Yoon, *J. Hazard. Mater.*, 2009, **168**, 346–351.

57 O. S. Furman, A. L. Teel and R. J. Watts, *Environ. Sci. Technol.*, 2010, **44**, 6423–6428.

58 L. Zhou, N. Piekiel, S. Chowdhury and M. R. Zachariah, *Rapid Commun. Mass Spectrom.*, 2009, **23**, 194–202.

59 E. de Hoffmann and V. Stroobant, *Mass Spectrometry: Principles and Applications*, 3rd edn, John Wiley & Sons, West Sussex, England, 2007, p. 17.

60 NIST webbook, http://webbook.nist.gov/chemistry/form-ser.html.

61 K. H. Stern, *High Temperature Properties and Thermal Decomposition of Inorganic Salts with Oxyanions*, CRC Press, Boca Raton, FL, 2007, p. 66.

62 N. W. Piekiel, G. C. Egan, K. T. Sullivan and M. R. Zachariah, *J. Phys. Chem. C*, 2012, **116**, 24496–24502.

63 N. W. Piekiel, L. Zhou, K. T. Sullivan, S. Chowdhury, G. C. Egan and M. R. Zachariah, *Combust. Sci. Technol.*, 2014, **186**, 1209–1224.